Time-Resolved PIV Diagnostics to Measure Flow Field Exiting Methane-Fueled Rotating Detonation Combustor

Daniel L. Depperschmidt[1], Jonathan R. Tobias[2], Robert S. Miller[3], Mruthunjaya Uddi[4], Ajay K. Agrawal[5]
Department of Mechanical Engineering, University of Alabama, Tuscaloosa, AL, 35487

and

Jeffery B. Stout[6]
Aerojet Rocketdyne, Canoga Park, CA, USA

Corresponding Author Email: aagrawal@eng.ua.edu

Time-resolved particle image velocimetry (TR-PIV) is applied to measure the flow field at the immediate exit of a rotating detonation combustor (RDC) operating on methane fuel and oxygen-enriched air, and configured with a back-pressure choke-plate. The challenges inherent to obtaining temporally consistent and spatially-well distributed seeded flow in a highly-periodic, supersonic, reacting flow field are discussed. Likewise, various measures taken to accurately implement the diagnostic and yield analytical results are detailed. The discussion includes laser optics configuration to maximize laser intensity in the region of interest, and consideration of seeder design and various seed materials and sizes to yield optimized results. Results acquired at 50 kHz PIV acquisition rate are presented to show the flow-field in two-dimensions: axial and circumferential velocity components. Results show that while the flow is primarily axial, a significant circumferential velocity component is also present. The flow oscillates in both directions with the passing of an oblique-shock structure in the PIV region of interest. Recommendations to improve the consistency and precision of the system for future studies are noted.

Introduction

IN a typical combustion process, fuel's chemical energy is converted to thermal energy which is then used to generate power by employing one of the many heat engine cycles. While the combustion efficiency is often close to 100%, the conversion from heat to work is usually inefficient resulting in low thermal efficiency depending upon the application. For example, the thermal (fuel) efficiency of Rankine cycle based power plants is in high 30s, while the gas-turbine/steam turbine combined cycle can yield fuel efficiency in excess of 60%. Efforts to surpass these targets pose enormous technical and practical limitations. In recent years, pressure gain combustion or PGC has received attention since it offers the potential to convert fuel's chemical energy to thermal energy in addition to increasing the pressure, which must otherwise be raised mechanically. Thus, PGC can substantially increase the fuel (thermal) efficiency for power generation and other similar applications.

Numerous methods to achieve PGC have been explored, but detonation based concepts such as pulsed detonation combustion (PDC) and rotating detonation combustion (RDC) are particularly attractive. In PDC, the detonation propagates linearly which requires intermittent filling (reactant mixture), combustion, and exhaust steps. Intermittent operation introduces prohibitive requirements such as fast response inlet valves, rapid and uniform fuel-air mixing, and control of limit cycle oscillations at low-frequency [1]. However, in RDC, detonation occurs continuously in the

[1] Graduate Research Assistant, Mechanical Engineering, dldepperschmidt@crimson.ua.edu, AIAA Member.
[2] Graduate Research Assistant, Mechanical Engineering, jrtobias@crimson.ua.edu, AIAA Member.
[3] Graduate Research Assistant, Mechanical Engineering, rmiller16@crimson.ua.edu, AIAA Member.
[4] Assistant Professor, Mechanical Engineering, uddi@ua.edu, AIAA Member.
[5] Robert F. Barfield Endowed Chair, Mechanical Engineering, aagrawal@eng.ua.edu, AIAA Associate Fellow.
[6] Project Engineer, Advanced Combustion Devices, AIAA Member

circumferential direction which can greatly simplify the combustor hardware. Though first conceived in the 1960's by Voitsekhovskii and Nicholls [2-3], research on RDC has intensified in recent year [4-8] because of its simplicity and the potential for higher thermal efficiency. In RDC, single or multiple co-rotating (or even slapping) detonation wave(s) exist at wave velocities exceeding 2,000 m/s (or >5,000 Hz), depending upon the reactants and operating pressure and temperature. Note that the combustor hardware to accomplish RDC is referred to as Rotating Detonation Engine (RDE) and the two terms, RDC and RDE are used interchangeably throughout this paper.

Figure 1 illustrate the typical flow processes inside an RDC. Fuel and oxidizer manifolds supply reactants axially at the base of the combustor annulus, through discrete fuel and oxidizer holes. Fuel and air mix rapidly to form the reactant mixture. A high energy ignition source is used to initiate deflagration to detonation transition (DDT) of the reactant mixture, and once detonation is established, it propagates continuously in the circumferential direction, i.e., normal to the reactant supply direction. In the reference frame of the detonation wave, the reactants ahead of the wave front are quiescent (circumferentially), and the products behind the detonation wave rotate away from the wave front; the temperature and pressure increase first by shock compression of the reactants and then by heat release across the reaction zone. The mass conservation dictates the rotating products to accelerate and turn axially across an oblique shock wave that rides above the detonation wave in the annulus. For high reactant flow rates, the process repeats itself resulting in multiple detonation/oblique shock waves. In both cases, reactants are injected without complex control devices or mechanisms. The cycle frequency is dependent on the mode of operation including single wave, multiple wave, and opposing orientation or "slapping wave" configurations [9-10]. The mode of operation is function of combustor geometry, injection plate design, reactant flow rates, etc. Experiments have shown that the wave velocity can reach up to 80 to 85% of the Chapman-Jouguet (CJ) velocity.

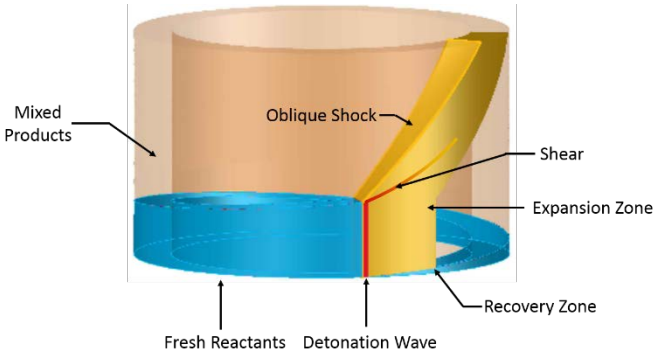

Figure 1. Schematic detailing flow processes within RDE.

The flow field inside the RDC is highly periodic even though the detonation occurs continuously. The so-called pressure gain is realized only in a small region across the rotating detonation wave in an otherwise periodic flow field generated at the base of the RDC. In this periodic flow, axial, radial, and circumferential velocities, and scalar properties such as pressure, temperature, and species concentrations vary with time and space. The pressure pulse can couple with the fuel and oxidizer supply lines and/or create backflow into the supply plenum(s). Thus, current RDC designs impose a large pressure drop penalty in the reactant supply lines to avoid the coupling, but it also reduces the benefits of PGC. Moreover, fuel and oxidizer are supplied separately to minimize the risk of the flashback, and thus, fuel-air mixing at the base of the annulus must take place rapidly and vigorously. The periodic flow at the annulus base may remain so throughout the RDC annulus, making it difficult to reduce the frictional loss to retain the pressure gain. The flow exiting the RDC must also be conditioned to supply a uniform flow at the downstream turbine inlet.

Many studies have been conducted to investigate the governing mechanisms of RDC and the corresponding flow field downstream of the primary combustion zone in efforts to optimize RDE's for practical applications. Computational based studies often focus on characterization of losses associated with high pressure injection systems and shock propagation downstream of the primary combustion zone. Schwer and Kailsanath [11] developed a numerical method of modeling RDC flow fields including characterization of potential losses due to imperfect detonation and propagation of shocks in the products. Paxson [12] created a simplified 2D model of a RDC with a coarse grid to reduce the computational cost while still comparing favorably with the more complex simulations. Rankin et al. [13] conducted studies of a RDE combustor with a nozzle integrated downstream of the combustor, and found that the nozzle was effective in reducing the periodicity of the flow at the nozzle exit. Kaemming et al. [14] developed a reduced-order model of the thermodynamic cycle of a RDE to provide a closer inspection of loss mechanisms such as imperfect detonation and varied injection area.

Numerous experimental studies have also been conducted on RDE technology. The group at Air Force Research Lab has engaged in extensive research [15-20] including parametric studies over multiple flow conditions and with various diagnostic techniques including chemiluminescence to characterize the reaction zone within the annulus [17, 20], and schlieren imaging to detail the dynamic coupling between the detonation wave and the fuel plenum [18]. Additionally, specific thrust measurements were acquired as nozzle configurations were varied, finding stagnation pressure rise of between 3% and 7% at certain equivalence ratios [19]. Performance based studies have also been

conducted by Sousa et al. [21] and Kawalec and Wolanski [22-23]. Studies involving RDC operation using higher carbon fuels such as CH_4 and other natural gas derivatives are important for land-based power generation applications, for example, involving combined gas turbine/steam turbine cycle systems. The present paper represents a series of studies by The University of Alabama (UA) research team to characterize natural-gas fueled RDCs for power generation [24-25].

The periodic RDC flow field is generally described by pressure, acoustic, and charge (ion) oscillations measured by high-frequency probes mounted on the wall(s) of the RDC annulus. In recent years, optical probes such as tunable-diode laser absorption spectroscopy (TDLAS) have been employed to measure species and/or temperature at high sampling rates, but along a line of sight. Although these various probes do provide accurate measurements of the wave velocity, the quality of the actual signal (spatially-resolved dynamic pressure, total pressure, temperature, or species concentration) is compromised by the physical size and related limitations in mounting and cooling the probe hardware. Thus, in spite of the extensive work to characterize the RDC operation, much more still needs to be ascertained. In particular, direct measurements of the periodic RDC flow field have not been obtained so far. Intrusive probes inherently disturb the flow field and thus, cannot be used to acquire the velocity measurements.

Particle image velocimetry (PIV) is the most common non-intrusive technique whereby the flow field is characterized by introducing seed particles in the flow and tracking them as they traverse through a laser sheet [26-28]. PIV technique requires small seed particles uniformly distributed across the flow and accurately following the flow. The seed particles must be large enough to scatter sufficient light that can be detected by the camera. The amount of light scattered also depends upon the laser sheet density, requiring high power laser(s) to illuminate the region of interest (ROI) precisely in synchronization with the camera shutter opening. In PIV, two images are acquired at a known (and short) time interval to track the particle motion related to the flow velocity. In a typical PIV setup, a single camera is oriented perpendicular to the laser sheet and the two velocity components aligned with the laser sheet are resolved based on the assumption that the seed particles do not cross the laser sheet when the two images are acquired.

PIV is an established technique used extensively to measure the flow field for a range of applications. However, much of the prior PIV research has utilized high-power lasers operated at low sampling rates, i.e., < 50 Hz. PIV measurements have been acquired in both non-reacting and reacting flows. However, there are many challenges associated with obtaining PIV measurements in high-speed reacting flow fields. For example, in supersonic, compressible flows, shock and expansion waves introduce localized regions of high acceleration and/or deceleration [29]. Thus, seed particles do not follow the flow accurately, and result in inconsistent seed density and/or seed agglomeration. In this case, the seed particle velocity may not represent the true flow velocity. Reducing the seed size can help, but it requires much higher laser sheet density to produce sufficient scattered light. Additionally, because of the high temperatures and pressures associated with supersonic combustion processes, the choice of seed particles is often limited to ceramics which will not deteriorate or react in such an environment.

In recent years, the advent of high repetitive rate lasers and high-speed digital imaging systems have led to the development of the time-resolved (TR) PIV. TR-PIV has become a powerful technique to investigate turbulent flows since measurements can be acquired relatively quickly. Studies based on TR-PIV have become increasingly routine, but most of them are still limited to PIV sampling rates of less than 10 kHz. In high speed reacting flows, the TR-PIV is still fraught with the above mentioned seed related issues, and thus, only a few PIV studies of supersonic, reacting flow fields are available in the literature [27, 29]. The high velocity RDC flow field is laden with shock and expansion waves at high temperatures and pressures, and additionally, it presents a new challenge not addressed in any of the prior PIV studies: the flow field is highly periodic with flow velocities varying intensely in time and space. This configuration not only exasperates the seed related problems, but also imposes the requirement of even higher power lasers that can operate reliably at repetitive rates much greater than 10 kHz. This study presents the steps taken to acquire velocity measurements in an RDC operated on methane fuel. PIV system was systematically analyzed and optimized to maximize the laser sheet density at PIV sampling rates of up to 50 kHz. Procedures to optimize the camera focus, and to precisely control the timing sequence of the experiment, camera, and laser were identified. Seed particles of different materials and sizes were tested to determine the best option(s) to acquire the 2D velocity field at the RDC exit. Lessons learned and plans for improvements in future studies are discussed.

I. Experimental Setup

The RDC experimental setup in the Engine and Combustion Laboratory (ECL) at UA has been discussed in detail by Tobias et al. [25] and Welch et al. [24]. This section will elaborate on setup details pertinent to this study. Figure 1 presents a cross-sectional view of the RDC at UA. The fuel and oxidizer flows meet the separate manifolds at the bottom of the RDC, and then enter the combustion annulus through injection holes on a specially designed mixing plate. The outer diameter of combustor annulus is 10 cm and the annular gap is 1 cm. The RDC design by Aerojet

Rocketdyne (AR) is modular by nature, and each of three spool pieces is tapped to mount multiple sensors for data collection during operation. Shown in Fig. 2 are pressure capillary (PC) and capillary tube averaged pressure (CTAP) ports to acquire static pressure measurements. A converging-diverging choke plate is located at the exit of the combustor annulus to simulate the back pressure expected in a RDC integrated with the gas turbine. The RDC is oriented vertically within a Lexan enclosure for safety, indoors within a test cell in ECL.

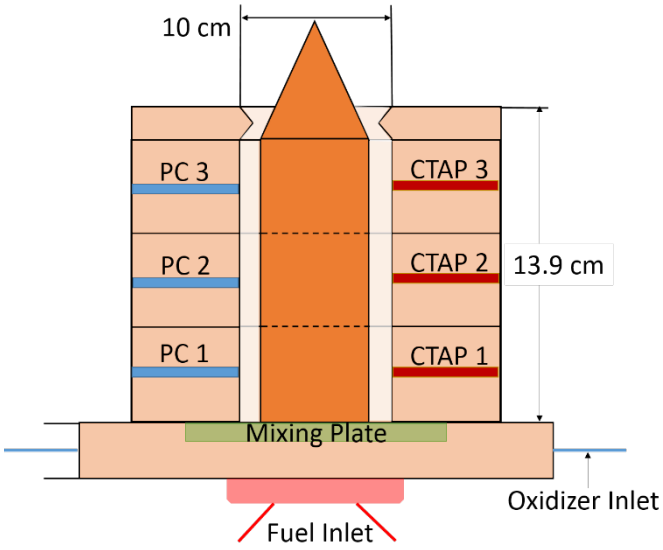

Figure 2. Bisectional diagram of the rotating detonation combustor.

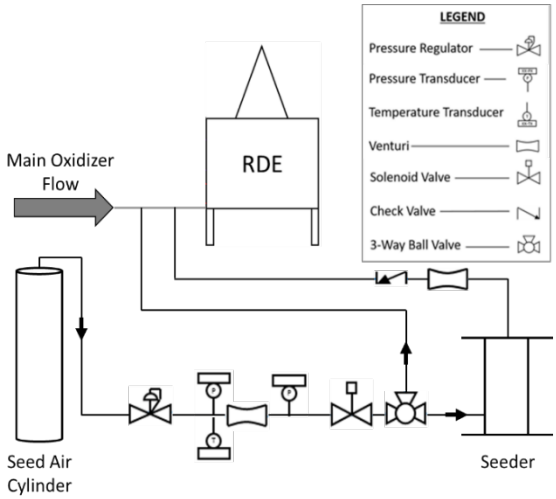

Figure 3. P&ID diagram detailing integration of seeder to flow system.

established at the immediate exit of the combustor annulus at a location both centered with respect to the width of the annulus channel and perpendicular to the camera. The region of interest correlated to a chord bisecting the annulus exit. This will be discussed further in detail in later sections of this study.

Each of the main reactant lines is equipped with a dome regulator to control the supply pressure and a fast acting electro-pneumatic (EP) valve to actuate the flow. The mass flow rate of each reactant is monitored by a critical venturi assembly including pressure and temperature transducers upstream of the venturi and a pressure transducer downstream to verify the choking of the flow. Test durations are restricted to ~0.60 sec to minimize potential damage to the hardware and diagnostic equipment. All operational components and diagnostic acquisitions sequences must be controlled with high precision. The timing sequence and triggering of all experimental events are controlled by an in-house built BeagleBone Black microprocessor-based system. Figure 3 presents a schematic of the seed air supply system. The seed air supply line is regulated in a similar fashion to the main reactant lines. A 3-way manual ball valve is used to bypass the seeder if necessary. The seeded airflow exits from the top of the seeder and passes through a non-critical venturi and a check valve before joining the main flow through a T-junction.

While multiple tests detailed in this section were conducted to closely examine and optimize laser diagnostics using a Quantronix Hawk Duo, 120 W, 532 nm Nd-YAG laser, the results presented in later sections were obtained with a Photonics DSH-532-35 laser system. The tests will be repeated with the new laser system in the future to quantify important diagnostic components and further optimize the system. The laser system and camera were synchronized via a TSI synchronizer, and the images were processed in TSI Insight 4G software. Figure 4 presents a timing diagram to indicate the relationship between camera image acquisition and laser pulses at 30 kHz, one of the acquisition rates used in this study. The time delay between laser pulses was set to 1 µs. The imaging system is a Photron SA-5 high speed camera positioned 62 cm from the region of interest. A filter was applied to the camera to isolate scattered laser light at the wave length of 532 nm. The region of interest from which PIV raw images were captured was

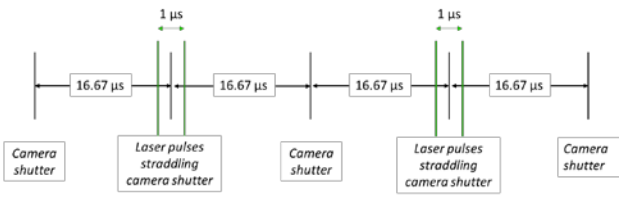

Figure 4. PIV timing diagram for 30 kHz

Next, steps taken to successfully acquire PIV data to characterize the flow field exiting the RDC will be discussed. To date, there has been minimal PIV analysis conducted on supersonic, reacting flow fields of this nature. This is in part due to the many challenges of applying a diagnostic technique reliant on a temporally consistent and spatially well-distributed seed flow capable of accurately responding to flow fluctuations with minimal delay. The diagnostic process is further complicated in a high-speed flow field undergoing expansion due to propagating reactions and shock waves as the products from the combustion events traverse from a high pressure environment to ambient pressure conditions. First, the necessary manipulation of the geometry of the laser sheet via optics to maximize laser sheet intensity will be detailed. Then, the measures taken to ensure that the timing of the laser pulses relative to the camera lens operation was optimized will be reviewed. Additionally, the steps taken to focus the high-speed camera properly to discreetly image particles on the nanometer scale given thermal lensing effects will be detailed. Finally, the consideration of appropriate seeding material and design of the seeder to deliver the required seed flow will be examined.

Laser Sheet Optimization

It is well documented that the seed particles, or tracers, 1) must accurately follow the flow with minimal discrepancy between particle velocity and the flow velocity, and 2) must provide excellent time response to rapid acceleration or deceleration in the localized fluid flow regimes. Small seed particles (diameters < 1μm) are required to properly characterize turbulent flows, however smaller seed particles reduce the light scattered. The relationship between particle diameter and the average energy of scattered light can be approximated by Eq. 1.

$$I = \left(\frac{d_p}{\lambda}\right)^2 \tag{1}$$

where I is the average energy of scattered light, d_p is the diameter of the seed particle, and λ is the wavelength of the incident light. Additionally, it is known that as the laser pulse frequency increases, the energy per pulse decreases. The assumed Gaussian profile of laser intensity will decrease significantly at high-speed acquisition rates compared to low-speed acquisition profiles. It was therefore required that the intensity of the generated laser sheet is maximized to ensure ample scattered light by seed particles.

Thus, a spherical lens and cylindrical lens combination was used to produce a laser sheet with height equal to the height of the region of interest (ROI), as determined by PIV acquisition rate and corresponding image pixel resolution, as well as distance of the high-speed camera from the ROI. Figure 6 illustrates the optical arrangement in Galilean collimator configuration to produce a laser sheet with minimal divergence. The beam first passes through a spherical lens with a focal length of 500 mm, constrained by the protective blast shield. The beam then traverses through a plano-concave lens with a focal length of -25 mm to produce an expanding sheet before entering a plano-convex lens with a focal length of 75 mm to generate a collimated sheet, and thus, to maximize the laser sheet intensity in the ROI. The laser sheet at the ROI must be thick enough such that a minimal quantity of seed particles enter/leave the sheet between the laser pulses. However, a thin laser sheet is required to maximize the energy density or light intensity. The laser sheet thickness was measured multiple times (three) by traversing a photodiode assembly across the sheet. Results revealed that the Gaussian distributed sheet was most intense across a thickness of about 1.1 mm. Therefore, a seed particle with a radial velocity (component normal to the laser sheet) exceeding 1,100 m/s will be lost, i.e., appear in only one of the two PIV images. Particle motion normal to the laser sheet can therefore be neglected for radial velocities half of this value, i.e., about 550 m/s.

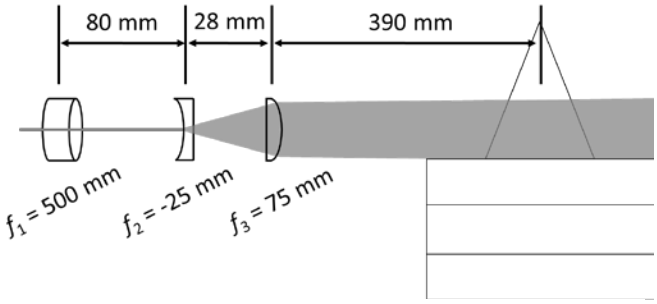

Figure 6. Diagram detailing laser optics arrangement used to maximize laser sheet light intensity at region of interest.

The time delay between laser pulses “A” and “B” (constituting the two images of the PIV image pair) was determined based on the expected flow velocities calculated from the reactant mass flow rate and adiabatic flame temperature. The computed axial velocity of about 600 m/s corresponded to a pixel displacement of 6.3 pixels over 1 μs given a pixel resolution of 95.24 μm/pixel. Additionally, best results are obtained when the laser pulses straddle the camera lens shutter symmetrically. Therefore, tests were conducted using a photodiode-oscilloscope assembly to

measure the laser pulse timing relative to the camera exposures. The tests were conducted for multiple timing settings, with parameters such as the amperage applied to the laser diode heads and the frequency of PIV capture were incremented to identify the proper settings for multiple diagnostic configurations. Because the laser output is Gaussian, it was expected that the peak light intensity would increase and that the full width half maximum (FWHM) length of the pulse would decrease as the amperage to the laser diode head was increased. When testing at a setting of 18 amp applied to each diode head and a PIV image frequency of 15 kHz, it was found that the FWHM of both pulse A and B were approximately 300 ns. At 28 amp and 15 kHz, the FWHM was reduced to ~150 ns for both pulses. Finally, with settings of 28 amp and 30 kHz, the FWHM for both pulses were measured to be 300 ns.

Camera Optimization

The ability to precisely focus the camera on the micron scale particles is paramount to high resolution velocity measurements. This was accomplished by adjusting the f-stop on the camera lens to a lower value (f/4) when focusing the camera on the ROI, and then changing it to a higher value (f/8) during the test. This allowed for a shallower depth of field during the focusing process prior to the test. The process consisted of generating the laser sheet at the same exact test location, but with a humidifier to introduce the seed particles to accurately focus the camera. Increasing the f-stop level increased the light throughput to the camera sensor during the test. The hot exhaust between camera lens and RDC assembly causes thermal lensing effect during the test and could distort the image focus compared to the non-reacting test environment. Increasing the f-stop during the test compensated for this thermal lensing effect. The camera focusing procedure reduced blur of seeded particles or seeded fluid structures.

Agglomeration of seed particles is a consistent challenge to PIV analysis. Seed agglomeration can be attributed to factors such as compression of tracers due to propagating shock events, where density and momentum gradients lead to particle collisions, coupled with the presence of water vapor in the products of combustion. After improvements made to the focusing process and to the laser sheet optics, a great percentage of seed particles could be recognized by the PIV analysis software.

Seeder Design

Appropriate design of the seeder delivery system is crucial to ensure adequate and consistent seed density, both temporally throughout the test duration and spatially throughout the region of interest. Additionally, a uniform seed size is preferred to avoid inconsistent or excessive light intensity from larger particles and background noise which would decrease the measurement accuracy [SR1]. Figure 7 illustrates a schematic of the self-designed seeder used in this study. As shown in Fig. 7, the air flows first through a section filled with marbles to supply a uniform flow at the bottom flange section. This section includes micron mesh to hold the seed and a swirler to promote fluidization of the seeded flow. The seeded flow exits the seeder via a ½" Swagelok union cross and ½" NPT Swagelok fitting before merging with the main oxidizer line. The seeded air line includes a non-critical venturi to accelerate the flow and thus, to break up seed agglomerates which commonly form in sub-micrometer diameter particles. Due to the short

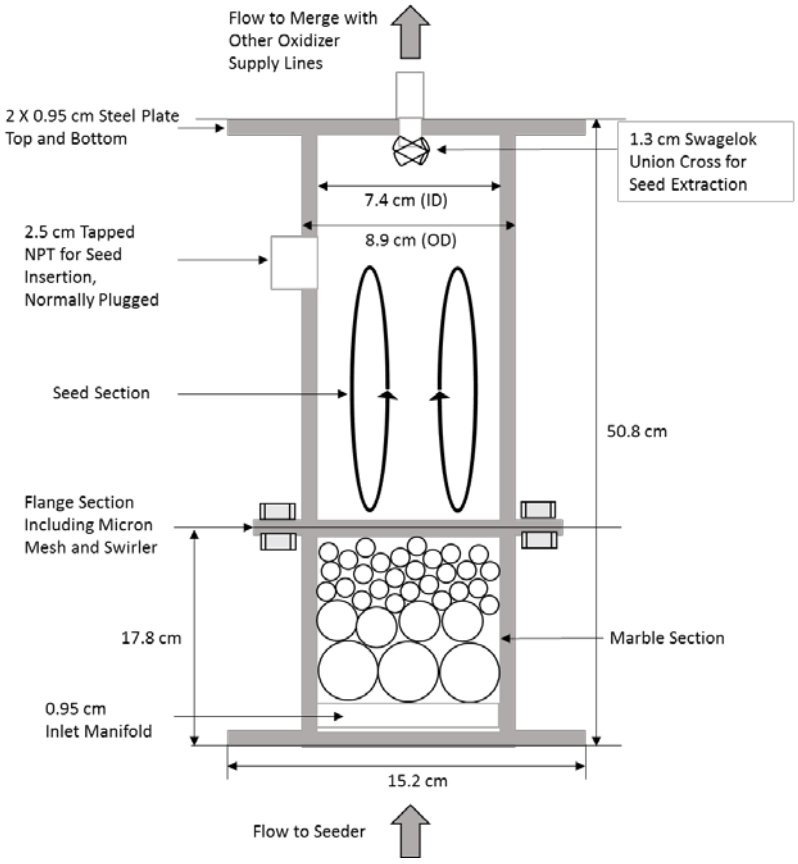

Figure 7. Bisectional schematic detailing design of seeder system used to generate fluidized, seeded flow for this study.

test durations (~0.6 sec), the seeder assembly could not employ a bypass design commonly used to toggle between seeded and non-seeded flow during the test. Instead, the seed-air line was set to flow through the seeder during the whole test duration when PIV measurements were acquired.

It was determined through multiple tests that the pressure of the seeded flow must be sufficiently higher than the main air and oxygen pressures to ensure proper mixing between the two flows. For low seed air supply pressures, the acquisition would often yield < 50 ms of images with spatially thorough seeding following ignition but decreasing in spatial density as the test progressed. It was postulated with high back pressure experienced by the combustion chamber annulus during the test, the seeded flow might now penetrate into the main oxidizer lines with significantly higher mass flow rates. This problem was partially remedied by decreasing the throat diameter of the sonic nozzle in the seed airline and thus, increasing the supply pressure of the seed air.

II. Results

In this section, the results of the application of the PIV diagnostic technique to the exhaust flow of a RDC will be discussed. While the results of the process of quantifying the precision of the laser system discussed previously was conducted with a Quantronix Hawk Duo, 120 W, 532 nm Nd-YAG laser, the results presented in this section were conducted with a Photonics DSH-532-35 laser system.

Variance of Seed Size/Material

In this study, multiple seed tracer types were used to inspect the effects of seed size and material on the ability to resolve the RDC exhaust flow field. The seeds tested were 1) 40 nm TiO_2, 2) 20-30 nm SiO_2, and 3) 200 nm ZrO_2. The results from the TiO_2 and SiO_2 powders will be discussed first. Figures 8a-d and 9a-c present raw PIV images acquired during combustor operation.

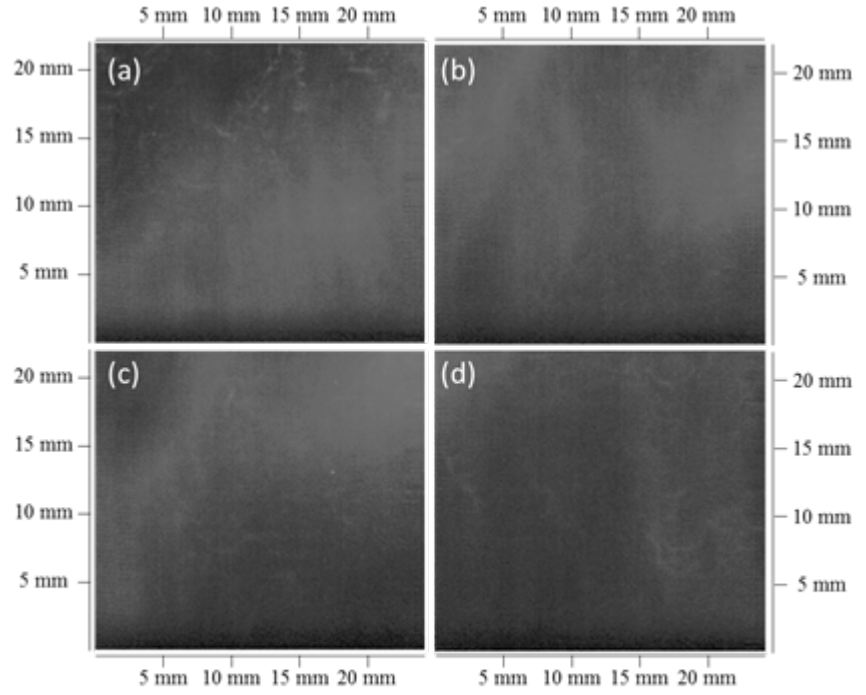

Figure 8a-d. Raw PIV images from tests of 40 nm TiO_2 seed tracers acquired at PIV acquisition rate of 50 kHz; images are first image of image pair progressing from a-d.

In both figures, images shown represent the segment of a cycle in which the attached oblique shock is passing through the field of view of the high-speed camera. In figure 8(a), the seed encompasses the entirety of the field of view. However, the seeded flow appears as a bulk fluid structure with little to no differentiation between particles. Additionally, gradient of light intensity within the bulk structure is not observable. The analysis software to compute the velocity vectors depends on its ability to differentiate between scattered light and ambient noise. The images shown in fig. 8a-d and the corresponding difficulty to analyze the resulting data were consistent for multiple tests using TiO_2 seed particles.

Figure 9a-c displays the results from tests using the SiO_2 tracers for PIV acquisition at 30 kHz, in an attempt to increase laser energy per pulse. Per manufacturer calibration data, the Photonics laser system is able to provide 0.91 mJ/pulse at 30 kHz as opposed to 0.76 mJ/pulse at 50 kHz. However, the results observed with the 20-30 nm SiO_2 seed were similar to those observed with 40 TiO_2 seed. Seed agglomerations form a bulk fluid structure, lending no quantifiable difference in light intensity between what the analytical software interprets as noise and peak spot intensity. The inability to properly conduct PIV with these small seed sizes is likely due to the insufficient light scattering from the

seed. This problem can be remedied by increasing the light intensity of the laser sheet or by increasing the size of the seed diameter, as given by eq. 1. Therefore, further tests were performed with 200 nm ZrO_2 seed particles.

Effect of Mass Flow on Periodicity

It is desirable to perform tests at conditions with minimal cycle-to-cycle variations. Previous studies conducted on the RDC configuration of this study found that the wave speed (and the corresponding cycle frequency fluctuations are reduced at elevated mass flow conditions [24]. This conclusion is supported by pressure data acquired by high-speed PCB probes in this study. Figure 10a&b show the spectragram plots based on dynamic pressure measurements.

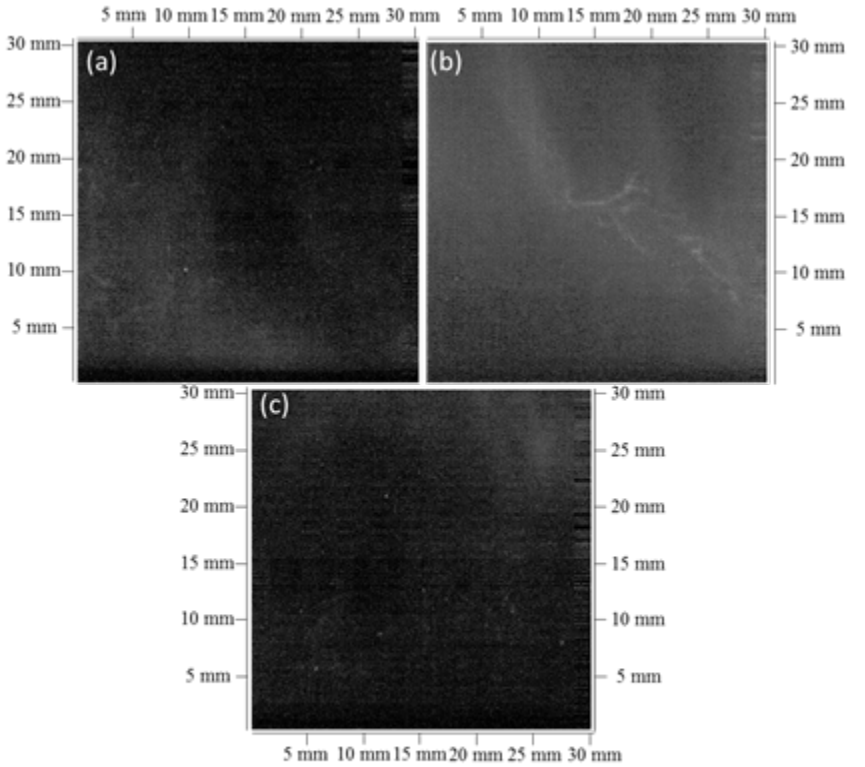

Figure 9a-c. Raw PIV images from tests of 20-30 nm SiO_2 seed tracers acquired at a PIV acquisition rate of 30 kHz; images are first image of image pair progressing from a-c.

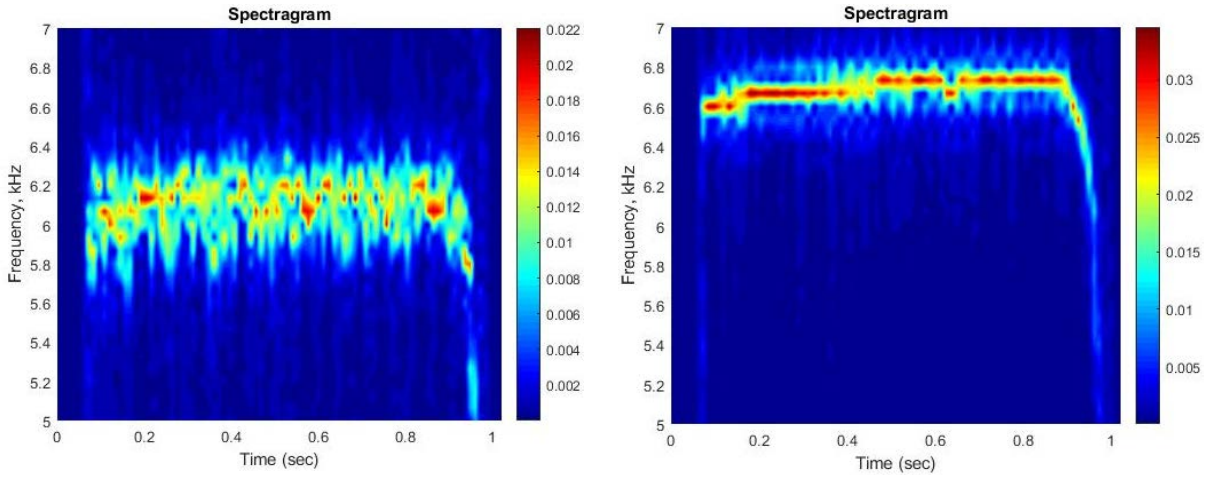

Figure 10a&b. Spectragram showing power density frequency of pressure fluctuations vs. time for: (a) $\dot{m}_{CH4}$ =0.0467 kg/s and (b) $\dot{m}_{CH4}$ =0.0726 kg/s conditions.

The lower mass flux test case, with an overall peak frequency of 6.129 kHz, shows significant cycle-to-cycle wave speed fluctuation throughout the test duration. On the contrary, the higher mass flux test case showed much more consistent cycle-to-cycle wave speed at an overall peak frequency of 6.715 kHz. While the actual cause for the periodic fluctuations is unknown at this time, the higher reactant flow rate is likely recuing the pressure coupling between RDC annulus and upstream supply lines. Of note in the $\dot{m}_{CH4}$ = 0.0726 kg/s test case is the apparent discrete segmented increases of frequency power density distribution. This may be attributed to thermal losses decreasing throughout the test duration as the temperature of the combustor annulus walls increase. PIV was therefore conducted for the higher flow rate test case.

High Flow Rate Test Case

The reactant flow rates for the high mass flow test case are: 0.0726 kg/s for methane, 0.0251 kg/s for O2, 0.152 kg/s for main air, and 0.0119 kg/s of seeded air flow. This corresponded to an equivalence ratio of ϕ=1.018. 200 nm ZrO2 powder was used as the seed tracer for 50 kHz PIV acquisition rate. Images acquired at this sampling rate correspond to a pixel resolution of 256 wide x 232 tall. The Photron SA-5 camera was positioned to obtain spatial resolution of 95.24 μm/pixel, and ROI of 24.38 mm x 22.10 mm. PIV images were processed using a starting spot size of 96x96 pixels, and a final spot size of 48x48 pixels.

The velocity measurements were analyzed via single point inspection, wherein nodes of the PIV interrogation grid close to the centerline of the PIV region of interest were selected and the velocity fluctuations over time at these point were interpreted. Inspection of points close to the centerline of the images acquired across the chord of the annulus perfectly normal to the high speed camera allows for the approximation that all non-axial velocity components are purely circumferential, and contain no radial velocity component. Figure 11a-c illustrates the three velocity components as they would be perceived from the top view (fig. 11a&b) and the front view (fig. 11c) of the RDE. In this study, all PIV measurements were acquired along a chord of the exit of the combustor annulus (fig. 11b&c), centered with respect to the width of the RDE. Here, all seed displacement measured in the "x" direction of the two-dimensional PIV images acquired can be assumed as $v_x = \sqrt{v_{circum}^2 + v_{radial}^2}$, where at $x = 0$; $v_{radial} = 0$. Therefore, as seen in fig. 11c, the assumption that all non-axial velocity measurements have no radial component is valid at the centerline of the field of view and inherits increased uncertainty as nodal locations are inspected further away from the centerline of the image. This assumption can be validated by conducting PIV measurements in the radial profile alignment (fig. 11a), in which radial velocities can be isolated and quantified. This test is planned for future studies.

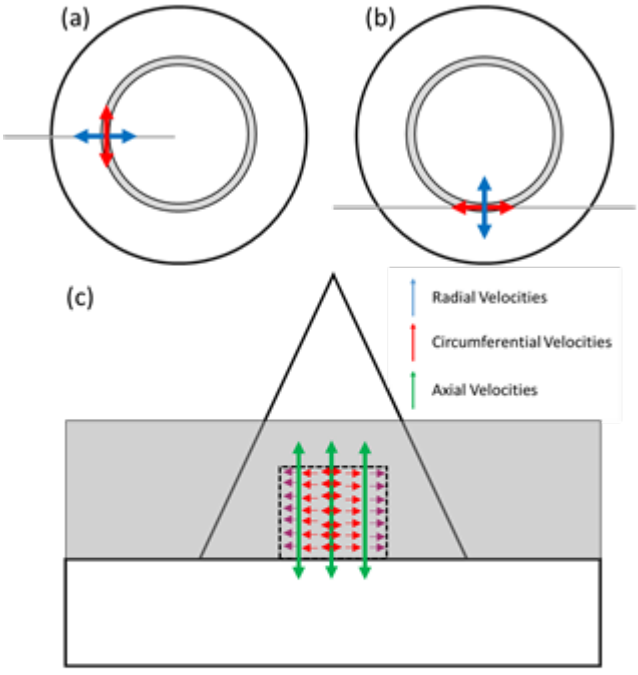

Figure 11. Illustration of velocity components in (a) top view of theoretical radial profile not used in this study, (b) top view of chord location used in this study, and (c) front view of chord location used in this study immediately downstream of combustor annulus.

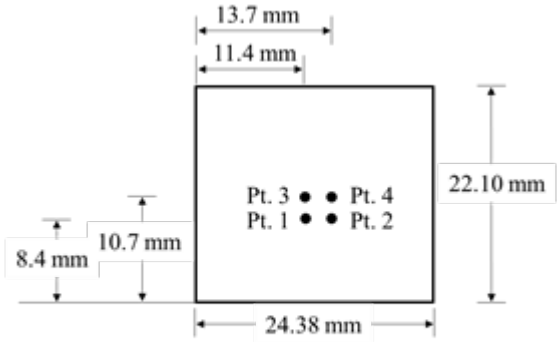

Figure 12. Location of points for PIV analysis for $\dot{m}_{CH4}$=0.0726 kg/s test case.

The location of the four points within the field of view is illustrated in figure 12. The bottom of the field of view corresponds to the exit of the back pressure plate located immediately downstream of the RDC annulus. At each point, 1030 image pairs were analyzed, starting with the image pair immediately following the detonation event. This selection of data therefore comprises 20.6 ms of test data. A significant amount of unsteadiness is expected in the period immediately following the ignition of the combustor, prior to quasi-steady state operation is acheived. For this test, the combustor operated in a single detonation wave mode, propagating in a clockwise (CW) orientation as measured by ion probe detectors.

Figure 13 presents the resulting velocity vs. time measurements at the four discrete nodal locations shown in fig 12. The resulting data were filtered to remove extreme outliers, including points where extremely low (< 25 m/s) and high (axial velocities > 3,000 m/s and circumferential velocities > 2,000 m/s) velocities were detected. Note that

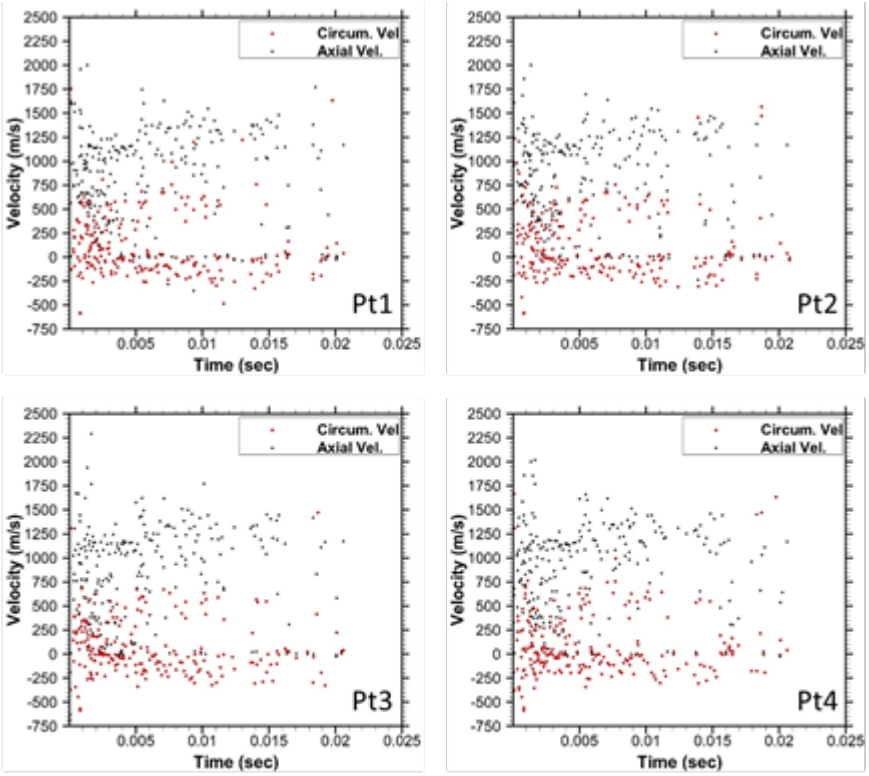

Figure 13. Resulting circumferential and axial velocity measurements vs. time for the $\dot{m}_{CH4}$=0.0726 kg/s test case. Results from PIV acquisition rate of 50 kHz using 200 nm ZrO_2 seed. Measurements at Pt. 1 (11.4 mm, 8.4 mm), Pt. 2 (13.7 mm, 8.4 mm), Pt. 3 (11.4 mm, 10.7 mm), and Pt. 4 (13.7 mm, 10.7 mm).

negative circumferential velocity values correspond to flow in the counterclockwise (CCW) orientation, while positive circumferential velocity values correspond to CW oriented flow.

Axial velocities were mainly between 250 m/s and 1,500 m/s, with some outliers observed. The vast majority of measured velocities were positive, with values close to 0 m/s inherently more susceptible to increased uncertainty. Circumferential velocity was between -250 m/s (CCW) and 750 m/s, suggesting that the flow field changes circumferential orientation during operation. Measurements at the four discrete locations are consistent with each other.

PIV acquisition at this test condition presented multiple challenges. Portions of the PIV images had unresolved vectors at all four locations. This outcome is attributed to segments of the flow without adequate seeding, possibly due to the inherent flow unsteadiness immediately after ignition. Additionally, seed quality abruptly dropped off after ~0.02 sec as shown in fig. 13. This is believed to be due in part to the inability of seeded flow to properly penetrate into the main oxidizer flow line. Therefore, PIV was also conducted at a lower mass flow rate.

The lower mass flow rate test case consisted of 0.0467 kg/s of CH_4, 0.159 kg/s of O_2, 0.0912 kg/s of main air, and 0.00894 kg/s of seeded air flow. These flow rates correspond to an equivalence ratio of ϕ=1.038. PIV was again acquired at 50 kHz with a region of interest of 256 x 232 pixels of same spatial resolution as before. Data was analyzed in a similar manner to the previous test condition, in which four discrete nodal locations were selected and the velocity fluctuations during the test were inspected. Due to the change in the final spot size, the discrete nodal locations of measurement changed. Figure 14 illustrates the measurement locations for this test case. Figure 15 presents scatter plots of the results for the four test points.

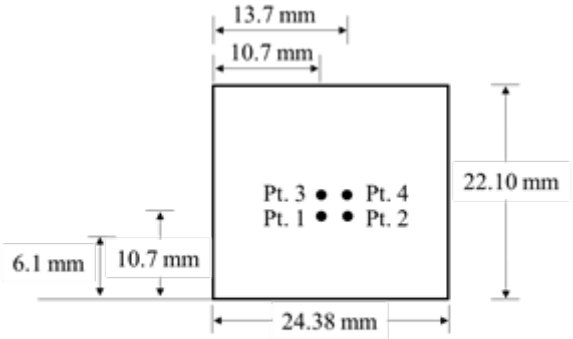

Figure 14. Location of points for PIV analysis for $\dot{m}_{CH4}$=0.0467 kg/s test case.

Ion probe measurements indicated a single detonation wave mode propagating in the CCW orientation. The plots show a higher density of resolved vectors than the higher mass flow rate condition. The axial velocities were mostly between 300 and 1,100 m/s. Circumferential velocity values were measured to be between 250 m/s (CCW) and -600 m/s (CW). Similar to the test case with higher mass flow rates, the highest values of the circumferential component of the flow were opposite to the direction of the propagating detonation wave. Quickly apparent from inspection of the scatter plots is a temporal inconsistency in resolved velocity vectors. This again is attributed to inconsistent seeding due to improper penetration of the seeded flow. Given the periodic nature of the absent velocity values and inadequate seed, it is possible that pressure fluctuations are propagating upstream of the RDC into the supply lines.

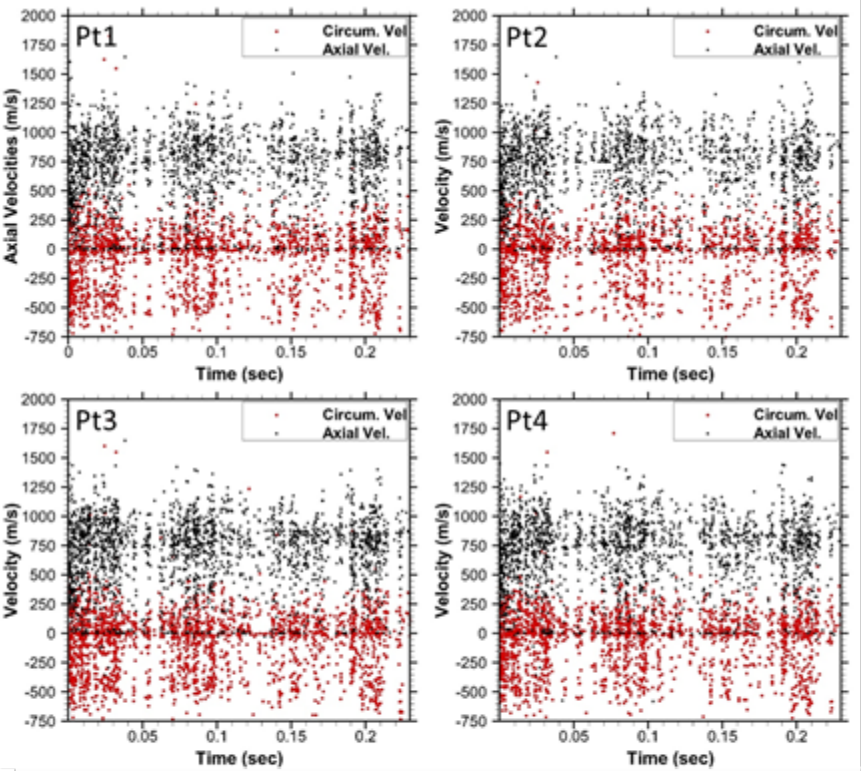

Figure 15. Resulting circumferential and axial velocity measurements vs. time for the $\dot{m}_{CH4}$=0.0467 kg/s test case. Results from PIV acquisition rate of 50 kHz using 200 nm ZrO_2 seed. Measurements at Pt. 1 (10.7 mm, 6.1 mm), Pt. 2 (13.3 mm, 6.1 mm), Pt. 3 (10.7 mm, 8.8 mm), and Pt. 4 (13.3 mm, 8.8 mm).

Figure 16a-h displays eight consecutive images, comprising 160 μs of the test, approximately equal to the average cycle duration (~163 μs) in order to closely inspect the PIV data. Each image represents a single image of the PIV image pair. The dark regime, shown vividly in images such as fig. 16f, represents the exit of the back pressure plate. As compared to the images displayed in figs 8 and 9, there is a significantly stronger contrast between seeded fluid structures and space in between. Additionally, in images in which the oblique shock is seen to be propagating CCW from the bottom left of the image to the top right, such as fig 16f&g, there is contrast between the peak light intensity of the fluid structures. This should allow for proper resolution of velocity measurements.

Figure 17a-h displays the velocity vectors corresponding to the images shown in fig 16a-h. As the seed particles associated with the shock structure in fig. 16e begin to propagate into the field of view, it is shown that the flow is largely axial but with a circumferential velocity component orientated in the direction of detonation wave propagation. In the same image, the seed particles immediately downstream (or in front) of the shock structure show orientation opposite to that of the detonation wave. As the shock wave passes through the field of view, the flow is turned to almost axial with much higher velocity magnitude. In fig. 17a-d, it is shown that the high magnitude flow turns from axial to a CW orientation with lower magnitude. This phenomenon is attributed to a rarefaction event of flow expansion in accordance with the conservation of momentum. This trend is continued in fig. 17d, in which the flow is shown to be oriented significantly in the CW orientation (and includes an outlier vector from a node at the top right of the image).

Of note, however, is the absence of resolved vectors in fig. 17h. To more closely inspect the cause of this omission in an image which appears to have adequate seeding, the image pairing is presented as fig. 18a&b. The inability of the computational software to properly resolve velocity vector measurements is determined to be the difference in light intensity from “pulse A” to “pulse B”, in which the fluid structures of fig. 18b (shown previously as fig. 16h) have significantly higher light intensity than those in fig. 18a. Additionally, while individual fluid structures can be discerned in fig. 18b, such as those in the top right corners of the image, in fig. 11a the same section of the image appears as light noise. These differences in the images provide a challenge for the computational software to properly correlate the displacement of lit pixels from image to image, and the result was an image pairing with no resolved vectors. Moving forward, the diagnostic would benefit from better balancing of the laser light intensity from image A to image B, and/or increased light intensity in image A.

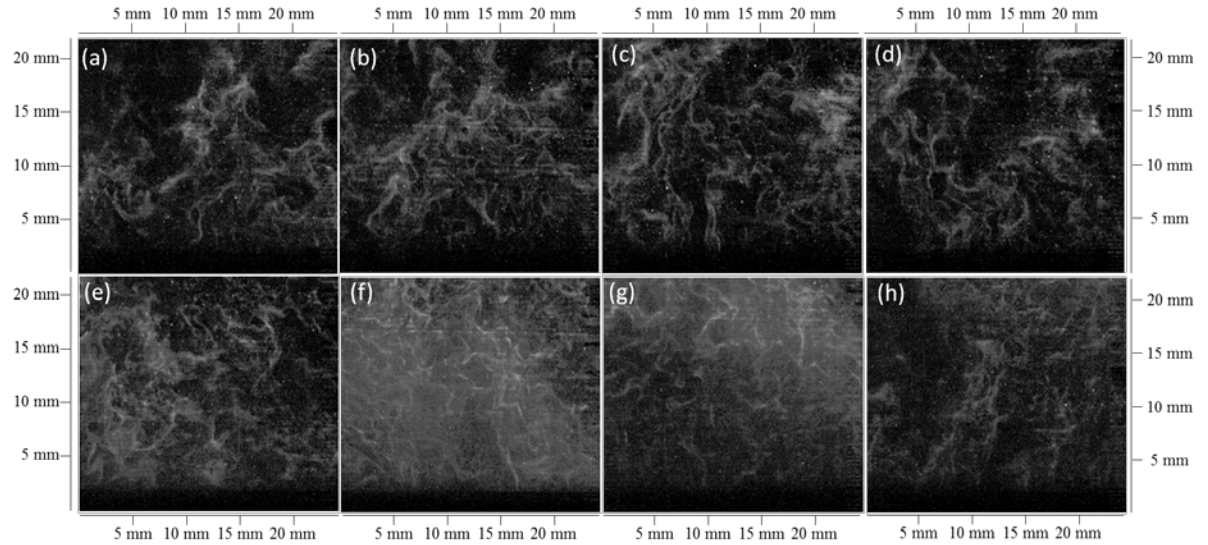

Figure 16a-h. Eight consecutive single images of PIV pair comprising approximate full cycle of test. Results from PIV acquisition rate of 50 kHz using 200 nm ZrO_2 seed. Images correspond to data 0.0245 sec after ignition.

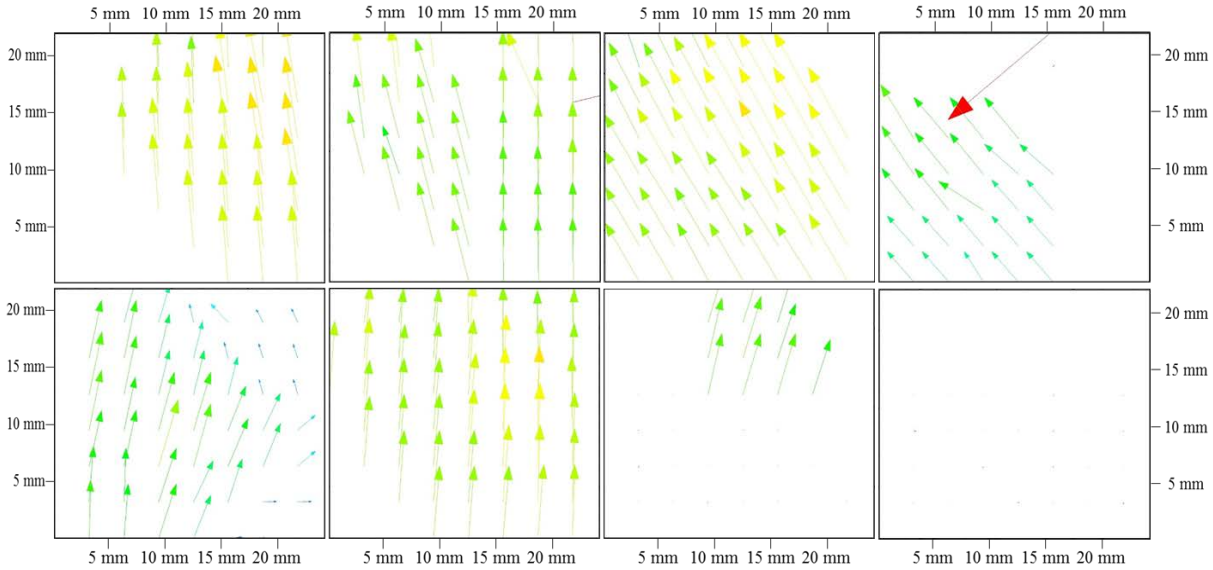

Figure 17a-h. Resolved velocity vectors of instantaneous flow field corresponding to the images of fig 8a-h.

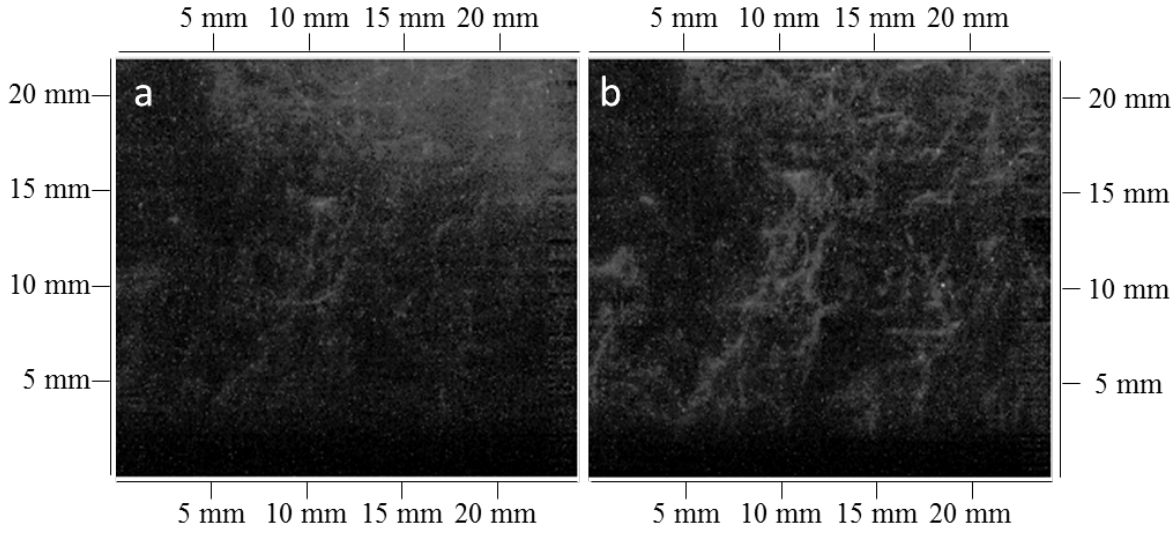

Figure 18a&b. Example of raw PIV image pairing in which no velocity vectors were resolved.

III. Conclusions

In this study, the challenges experienced while applying high-speed, time-resolved PIV to measure the highly periodic, turbulent, supersonic, reacting flow field at the exit of a rotating detonation combustor outfitted with a back-pressure choke-plate. The combustor was operated on methane fuel, and oxygen-enriched air mixture for two different flow rates in which the single-wave mode operated at dominant frequencies of 6.129 kHz and 6.715 kHz. Results were acquired using 200 nm ZrO_2 seed particles at a 50 kHz PIV acquisition rate and analyzed by inspecting the variation of the discretized two-dimensional flow field at single nodes within the PIV interrogation grid. The study was successful in providing the following lessons and insights:

- Delivering an adequate supply of temporally consistent and spatially well distributed seed is a significant challenge given the complexity of the RDC flow field. The best results were obtained when the ratio of seed supply pressure to main oxidizer supply pressures was increased significantly by reducing the critical venturi on the seed supply line.
- Laser sheet light intensity must be maximized at the region of interest. This was achieved by implementing a Galilean collimator design. Additionally, small seed sizes (~40 nm) of TiO_2 and SiO_2 were ineffective in scattering enough light to distinguish between seeded structures and light noise. 200 nm ZrO_2 was effective in this regard.
- The higher flow rate test case showed less cycle-to-cycle wave speed fluctuations, however adequate seeding was limited to a short time duration following ignition. The lower flow rate test yielded more resolvable data, yet still showed variations in seed consistency.
- PIV results of the two-dimensional flow field showed that the flow field is highly periodic, with velocity fluctuations largely dependent on the passing of an oblique shock through the region of interest.
- While the flow is largely axial, a significant component of the local velocities is circumferential. This circumferential component oscillates between the orientation of the propagating detonation wave within the combustor annulus and counter to that orientation, depending on the time within the cycle relative to the passing of the shock.
- The higher flow rate test case showed measured axial velocities ranging between 250 m/s and 1500 m/s and circumferential velocities between 250 m/s in the same orientation as the detonation wave and 750 m/s in the direction counter to this orientation. The lower flow rate test case had axial velocities mainly between 300 and 1100 m/s, with circumferential velocities ranging mainly from 250 m/s in the orientation of the detonation wave to 600 m/s in the direction counter to that.

Moving forward, several improvements to the PIV diagnostic system can be made for future studies. Temporal seed consistency must be improved, potentially by reducing the effect of pressure fluctuations propagating upstream

from the RDC into the reactant supply lines. Laser light intensity between the two PIV image pairs must be matched properly. Experimental uncertainties related to seed size and relaxation time should be quantified and reduced. However, based on previous literature [29] this would likely require using smaller seed sizes and thus, higher laser power. Higher flow rate test conditions with reduced cycle-to-cycle fluctuations should be investigated further, but with ensuring consistent seed injection and distribution.

Acknowledgments

This material is based upon work supported by the Department of Energy under Award Number(s) DE-FE0023983.

References

[1] Roy, G.D., Frolov, S.M., Borisov, A.A., and Netzer, D.W., "Pulse detonation Propulsion: Challenges, Current Status, and Future Perspective," Progress in Energy and Combustion Science, Vol. 30, No. 6, pp. 545-672, 2004.

[2] Voitsekhovskii, B.V., "Stationary spin detonation," Sov. J. of Applied Mechanics and Technical Physics, No. 3, pp. 157-164, 1960.

[3] Nicholls, J. A., and Cullen, R. E., "The Feasibility of a Rotating Detonation Wave Rocket Motor," Univ. of Michigan, TR-RPL-TDR- 64-113, Ann Arbor, MI, 1964.

[4] Lu, F.K., Braun, E.M., "Rotating Detonation Wave Propulsion: Experimental Challenges, Modeling, and Engine Concepts". Journal of Propulsion and Power, 2014. **30**(5): p. 1125-1142.

[5] Wolanski, P., "Detonative Propulsion", Proceedings of the Combustion Institute, Vol. 34, pp. 125-158, 2013.

[6] Bykovski, F.A. and Zhdan, S.A., "Current Status of Research of Continuous Detonation in Fuel–Air Mixtures (Review)", Combustion, Explosion and Shock Waves, vol.51, no.1, pp.21-35, 2015.

[7] Kailasanath, K. "Recent Developments in the Research on Rotating-Detonation-Wave Engines", AIAA 2017-0784, 55th AIAA Aerospace Sciences Meeting, 9-13 January 2017, Grapevine, Texas.

[8] Rankin, B.A., Fotia, M.L., Naples, A.G., Stevens, C.A., Hoke, J.L., Kaemming, T.A., Theuerkauf, S.W., Schauer, F.R., "Overview of Performance, Application, and Analysis of Rotating Detonation Engine Technologies", Journal of Propulsion and Power, Vol. 33, Special Section on Pressure Gain Combustion (2017), pp. 131-143.

[9] Roy, A., Ferguson, D., Sidwell, T., O'Meara, B., Strakey, P., Bedick, C., Sisler, A. "Experimental Study of Rotating Detonation Combustor Performance under Preheat and Back Pressure Operation", AIAA 2017-1065, 55th AIAA Aerospace Sciences Meeting, 9-13 January 2017, Grapevine, Texas.

[10] Pandiya, N., St. George, A., Driscoll, R., Anand, V., Malla, B., Gutmark, E.J. "Efficacy of Acoustics in Determining the Operating Mode of a Rotating Detonation Engine", AIAA 2016-1649, 54th AIAA Aerospace Sciences Meeting, 4-8 January 2017, San Diego, California.

[11] Schwer, D.A. and Kailasanath, K., "Numerical Investigation of Rotating Detonation Engines," *46th Joint Propulsion Conference and Exhibit*, AIAA Paper No. 2014-0284, 2014.

[12] Paxson, D., "Numerical Analysis of a Rotating Detonation Engine in the Relative Reference Frame," *52nd AIAA Aerospace Sciences Meeting*, AIAA Paper No. 2014-0284, 2014.

[13] Rankin, B., Hoke, J., and Schauer, F., "Periodic Exhaust Flow through a Converging-Diverging Nozzle Down-stream of a RDE," *52nd AIAA Aerospace Sciences Meeting*, AIAA Paper N. 2014-1015, 2014.

[14] Kaemming, T., Fotia, M.L., Hoke, J., Schauer, F., "Thermodynamic Modeling of a Rotating Detonation Engine Through a Reduced-Order Approach," Journal of Propulsion and Power, Vol. 33, No. 5, September-October 2017.

[15] Dyer, R., Naples, A., Kaemming, T., Hoke, J., and Schauer, F., "Parametric Testing of a Unique Rotating Detonation Engine Design," *50th AIAA Aerospace Sciences Meeting including the New Horizons Forum and Aerospace Exposition*, AIAA Paper No. 2012-0121, 2012.

[16] Shank, J.C., King, P.I., Karnesky, J., Schauer, F., and Hoke, J.L., "Development and Testing of a Modular Rotating Detonation Engine," *50th AIAA Aerospace Sciences Meeting including the New Horizons Forum and Aerospace Exposition*, AIAA Paper No. 2012-0120, 2012.

[17] Naples, A., Hoke, J., Karnesky, J., and Schauer, F., "Flowfield Characterization of a RDE," *51th AIAA Aerospace Sciences Meeting including the New Horizons Forum and Aerospace Exposition*, AIAA Paper No. 2013-0278, 2013.

[18] Fotia M.L., Hoke, J.L., and Schauer, F., "Propellant Plenum Dynamics in a Two-dimensional Rotating Detonation Experiment," *52nd AIAA Aerospace Sciences Meeting*, AIAA Paper No. 2014-1013, 2014.
[19] Fotia M.L., Schauer F., Kaemming T., and Hoke J., "Study of the Experimental Performance of a Rotating Detonation Engine with Nozzled Exhaust Flow," 53rd AIAA SciTech Forum, Kissimmee, FL, 2015.
[20] Rankin B.A., Richardson D.R., Caswell A.W., Naples A.G., Hoke J.L., Schauer F.R., "Chemiluminescence imaging of an optically accessible non-premixed rotating detonation engine," Combustion and Flame 176, 2016, p. 12-22.
[21] Sousa, J., Paniagua, G. and Morata, E.C., 2017. Thermodynamic analysis of a gas turbine engine with a rotating detonation combustor. *Applied Energy*, *195*, pp.247-256.
[22] Wolanski, P., "Opportunities for the Future Turbine Engine with Detonation Combustion Chamber", Prace Instytutu Lotnictwa, Nr 3, 244, 2016, s. 202-214, Warszawa (in Polish)
[23] Kawalec M., Wolanski P., "Research of the Rocket Engine with Detonation Chamber," 26th ICDERS, 2017.
[24] Welch, C., Depperschmidt, D., Miller, R., Tobias, J., Uddi, M., and Agrawal, A.K., "Experimental Analysis of Wave Propagation in Methane-Fueled Rotating Detonation Combustor," ASME Paper GT2018-77258, 2018.
[25] Tobias, J., Depperschmidt, D., Miller, R., Uddi, M., and Agrawal, A.K., "OH* Chemiluminescence Imaging of the Combustion Products from a Methane-Fueled Rotating Detonation Engine", in Proceedings of ASME Turbo Expo 2018: Turbomachinery Technical Conference and Exposition, ASME Paper GT2018-77255: Oslo, Norway.
[26] Raffel, M., Willert, C., Wereley, S., Kompenhans, J., "Particle Image Velocimetry: A Practical Guide," 2nd Edition, Springer-Verlag Berlin Heidleberg, 2007.
[27] Scarano, F., Schröder, A., Willert, C.E., "Topics in Applied Physics: Particle Image Velocimetry, New Developments and Recent Applications: Overview of PIV in Supersonic Flows," Vol. 112, p. 445-465, Springer-Verlag Berlin Heidelberg, 2008.
[28] Adrian, R.J., "Twenty years of particle image velocimetry", Experiments in Fluids, Vol. 39, 2005, p. 159-169.
[29] Ragni, D., Schrijer, F., van Oudheusden, B.W., Scarano, F., "Particle tracer response across shocks measured by PIV", Experiments in Fluids, Vol.50, 2011, p. 53-64.